

Visualizing Dynamic Microvillar Search and Stabilization during Ligand Detection by T cells

En Cai^{†1}, Kyle Marchuk^{†1,2}, Peter Beemiller^{†1}, Casey Beppler^{†1}, Matthew G Rubashkin³, Valerie M Weaver³, Bi-Chang Chen⁴, Eric Betzig⁴, Frederic Bartumeus⁵ and Matthew F Krummel^{1,2*}

¹Department of Pathology, ²Biological Imaging Development Center and ³Center for Bioengineering and Tissue Regeneration, University of California, San Francisco, California 94143, USA. ⁴HHMI, Janelia Farm. ⁵ICREA Movement Ecology Laboratory, Center for Advanced Studies of Blanes, CEAB-CSIC, Girona, Spain.

*To whom correspondence should be addressed. Mail: matthew.krummel@ucsf.edu

[†]These authors contributed equally

Abstract

In searching opposing cell surfaces for peptide-MHC complexes, T cells must solve a classic search tradeoff between speed and sensitivity. It has long been supposed that small microvilli on T cell surfaces are used as sensory organs to enable this search, but their strategy has not been amenable to study. We used time-resolved lattice light sheet (LLS) and Qdot-enabled synaptic contact mapping (SCM) microscopy to show how microvilli, moving in random-walks on the surface of T cells, search opposing cells and surfaces prior to and during antigen-recognition. We uncovered fractal organization of the microvilli and found that their movements survey the majority of opposing space within one minute, with individual microvilli local dwell times sufficiently long to permit discrimination of pMHC half-lives. TCR recognition results in selective stabilization of receptor-occupied protrusions, and subsequent TCR movements take place upon the stabilized protrusions, even while transient ones test new regions. Intrinsic stabilization was independent of tyrosine kinase signaling and the actin cytoskeleton suggesting that the process selects for dense avid TCR microclusters. This work defines the efficient cellular search process against which ligand detection takes place.

One Sentence Summary: T cells use a dynamic fractal search pattern to palpate opposing surfaces; contacts that become occupied at high density by TCRs are stabilized, independently of signaling or actin.

Main Text

T cells utilize surface-bound T cell receptors (TCR) to identify ligands on antigen-presenting cells. Detection results in rapid intracellular signaling, necessary for acquisition of effector functions and for profound adaptive immunity. TCR recognition happens as surface deformations provide initial contact (1-9). but despite various fixed and lower-resolution approaches to understanding this process, it has not been possible previously to study this complete surface in real-time in the full 3-dimensions in which it takes place. In particular, it is not clear how surface deformation is used to make detection efficient and whether the entire initial deformed surface is stable as soon as contact is made or whether cells might continue to 'search' the surface in some form.

We imaged membrane deformations across the entire surface of T cells in culture at 0.22-0.44 Hz at diffraction-limited resolution using lattice light sheet microscopy(10) and using T cells that were surface-labeled with either monovalent non-stimulatory antibodies to the highly abundant surface molecule CD45 or a membrane-bound form of the fluorophore tdTomato. Microvilli were found to be highly dynamic structures (**Fig 1A** and **Movies 1-2**). Most microvilli undulate and translate, although we occasionally observed apparent reabsorption or projection from flatter membrane patches. We tracked translation and found that lateral displacements on the surface had a range of average speeds in individual cells (**Fig 1B**) with a mean across three cells of $5.2 \pm 0.4 \mu\text{m}/\text{min}$, which approximates the translation speed of T cell motility *in vivo*(11, 12). Microvillar movements covered a wide range of angles between timepoints (**Fig 1C**) with a close to uniform distribution of 82 ± 3 degrees ($n=3$), suggesting random turning. Plots of microvilli displacements versus the square root of time were nearly linear for the first ~15 seconds, also resembling free diffusion (**Fig 1D**). Over longer times, we noted a slight reduction in the slope of this line, suggesting that each microvillus might also be modestly confined within a larger patch of cell cortex.

The dynamics of microvilli were also visualized by sequential line-scans of a patch of membrane over three sequential timepoints (e.g. 9 seconds; **Fig 1E**) revealing tilting in addition to translation. However, when assessed over >1 minute period periods (**Fig S2A-B**) similar analysis did not support 'hot spots' for scanning, suggesting possibly underlying order that distributes these projections. We thus assessed microvillar distribution across length scales and time, performing fractal analysis. Fractal geometries in nature often provide consistent coverage across scales,(13) filling a volume or a surface in a compact and effective way, or assisting in finding adequate compromises between local exploitation and broad exploration(14). Plots of the logarithm of the number of regions that are necessary to contain all microvilli versus the logarithm of the region size gave a linear relationship across 1.5 orders of magnitude (**Fig 1F** and **S4A-B**), suggesting indeed that microvially distribution is fractal. Notably, the observed fractal dimension F_d varied little with time (example **Fig 1F, inset**), suggesting that both a stationary stochastic and a complex dynamic process governs efficient microvillar-based scanning.

To quantify how effectively these fractally distributed projections 'search' opposing surfaces, we first considered a randomly selected cell-contact sized regions just above the cell volume, in the absence of any surface-contacts at that site (e.g. Mask, **Fig 1G** and **Fig S1**). We then quantified the distributions of microvilli projected from the T cell into that mask, by applying a threshold to convert intensities into a binary map (Threshold, **Fig 1G**) using red to represent instantaneously 'occupied' space and black to represent 'unoccupied' areas. Further, to identify regions that have ever been scanned, we created a 'Cumulative' image in which red now represents space that had a microvillus at that site at any time (example in **Fig 1G** shows total coverage achieved within 13.5 seconds). We then generated time-series of these projections (**Movie 3**) and plotted the instantaneous and cumulative percent occupancy over time (**Fig 1H**). We found that cells had very consistent degrees to which they were instantaneously surveying such a region, here having an average of 39.8% and deviating less than 10% from this at any time (we observed variation in the mean coverage, cell-to-cell, from 35-45%, **Fig 2B**). Notably, apparently random movements of microvilli resulted in a very rapid rise in cumulative coverage over time; 98% of the putative surface was visited by at

least one microvillar contact within 1 minute (**Fig 1H**). For perspective, the half-life of T cell-APC contacts *in vivo* is roughly 1 minute (**Fig 1H**), suggesting that nearly complete scanning can be completed at physiological dwell times.

We next sought to determine whether membrane movements changed upon recognition of pMHC, presumably the goal for which the search is ideally tuned. We thus analyzed regions of the T cell surface that either were or were not in contact with the surfaces of opposing antigen-presenting dendritic cells (DC) bearing agonist pMHC complexes. An example of a T cell contacting a pMHC-bearing DC and the studied regions within ('IS') and outside ('non-IS') the synapse is shown in **Fig 2A**. We found that instantaneous coverage did not vary appreciably over the time-course of synapse development for either location and that IS versus non-IS regions were similarly dense for protrusions (**Fig 2B**) suggesting that T cells did not 'intensify' their search for antigens upon recognition. However a cumulative plot revealed that, in the IS, the rate of surface contact saturation actually slows down (**Fig 2C**). To capture this, we adopted a metric (T75%) that reports the time at which 75% saturation of the contact is achieved, based on the 75% coverage point lying at the steep part of the contact saturation curve. In the example cell shown in **Fig 2A**, we found T75% was significantly faster (13.5 seconds) in non-IS compared to IS (45 seconds) and IS regions were slower to saturate as a class, compared to either isolated cells that were not making contacts with other cells or when comparing non-IS regions in the same cells (**Fig 2D**).

We hypothesized that the reduced saturation rate in the IS was a consequence of some protrusions being stabilized as a result of ligand detection, therefore leaving fewer protrusions to scan new areas. To assess dwell time via LLS imaging from the perspective of the 'target', we developed an analytic method to analyze occupancy patterns at all the possible microvilli-sized (**Fig S3**) areas within a putative contact (**Fig 2E**). To extract how long such a region was continuously occupied by a T cell protrusion, we tracked the binary intensity of single-microvilli sized regions through time. A plot for a typical region is shown in **Fig 2F**, demonstrating times when microvilli passed through the region and exceeded a threshold of 50% coverage for just a single imaging timepoint (black arrow heads) or dwelled longer (grey arrow head). We plotted the average lifetime of all protrusions that were above the 50% cutoff for multiple cells and found similar lifetimes for isolated cells and for non-IS regions of cells that were engaging pMHC-bearing DCs (averaging 6.9 and 6.48 seconds respectively, **Fig 2G**). In contrast, average dwell times were longer in the IS (8.9 seconds). We differentially color-coded protrusions in image sequences for an IS region, based on whether they visually persisted (**Fig 2H** and **Movie 4**). This highlighted the more stable microvilli that ceased to scan as extensively in the IS. Such stable contacts were typically but not exclusively localized in the center of the contact.

These LLS data suggest stabilization of contacts might occur as a stochastic result of global signaling or as a specific consequence for those that had ligated their TCRs. We therefore sought to visualize TCR microclusters together with these protrusion structures, and while LLS imaging had proved facile for full cell volumes, we sought a companion tracking technique based on TIRF imaging as a means to increase the scanning rate at the IS and focus upon nanometer level measurements of the contacts. We also sought to simultaneously visualize membrane apposition together with TCR density. Therefore, we analyzed T cells that were settled upon supported lipid bilayers containing pMHC and ICAM (15, 16) to see if we could detect and thus study similar microvillar-like protrusions under these conditions. LLS imaging of fixed cells on bilayers (**Fig S5A** and **Movie 5**) also demonstrated that T cells generated microvillar-like projections. Scanning angle interference microscopy (**Fig S5B**) of T cells encountering lipid bilayers similarly confirmed that there were significant height variations of membrane for cells engaging lipid bilayers (**Fig S5C**). Notably bright TCR accumulations (microclusters) were closer to lipid bilayers as compared to the entire pool

average, which is consistent with very recent variable-angle TIRF studies showing TCR pre-enriched at microvillar tips(17). ICAM-1, a bigger molecule, was found farther away from the bilayer (**Fig S5B-D**).

To then study these contacts in real-time, we developed a method whereby quantum dots (Qdots), with a diameter larger than TCR-pMHC bond lengths, were seeded onto the lipid bilayers and used to specifically study close apposition on the scale of molecular interaction, akin to a 'molecular ruler'(18) (**Fig 3A and S6A**). When T cells engaged bilayers containing ~16 nm Qdots, we observed 'holes' in the otherwise uniform Qdot layer (**Fig 3B**) and found that intense TCR 'microclusters' were inversely correlated with the Qdot intensity (**Fig 3B-C**). We confirmed that the contact 'holes' and inverse correlation with TCR were specifically seen with larger 16 nm Qdots, but were essentially lost when smaller (~13 nm in diameter) Qdots or rhodamine formed the fluorescent layer (**Fig S6B-C**). These exclusion zones were likewise revealed when Qdots were added after synapses had formed (**Fig S6E**), showing that the Qdots did not induce the structures. We termed this method synaptic contact mapping (SCM) and found that SCM 'holes' had mean diameter of 541 nm (**Fig S6D**) as compared to LLS imaging which estimated the mean microvilli thickness at 540 nm (**Fig S3**). Also predicted from LLS imaging, these contacts could be observed to form as cells first spread onto bilayers (**Fig 3D and Movie 6**) and occurred at consistent densities over time (**Fig 3E**). We also applied SCM in a multichannel format to co-track multiple molecules alongside Qdots. TCRs co-localized with holes/contacts (**Fig 3B**) while LFA-1/ICAM, which are larger molecular interactions, were excluded (**Fig S7**).

'Holes' in the Qdot distribution were mapped using automated image analysis (**Fig S8**) and not all contact regions contained significant accumulations of TCRs (arrows in **Fig 3B box-inset** and **Fig 3F**). To quantify this and to determine whether TCR-occupied protrusions had longer dwell times in the IS, we defined a cutoff based on background TCR intensity levels across the entire imaging field (**Fig 3F**), and thereby defined 'TCR⁻' versus 'TCR⁺' contacts. We used 20 second windows of analysis to limit observations of rebinding and found that whereas TCR⁻ SCM 'holes' had a mean lifetime of 3.7 seconds, TCR⁺ SCM sites were stable for an average of 11.1 seconds (**Fig 3G**). Additionally, 25% of TCR⁺ SCM sites were stable for the entire observation period whereas none of the TCR⁻ contacts persisted. While we've long recognized stabilized TCR microclusters as a feature of a signaling interface, this analysis reveals an additional ongoing 'search' of the opposing surface that continues to take place, apart from microclusters (**Fig 3H and Movie 7**).

SCM also allowed us to study how 3D membrane dynamics underlie some of the movements of TCR microclusters that have previously been described.(15, 19) We used kymographs of TCR tracks to show an exact correspondence between complex TCR movements and the movements of the underlying 3D protrusion (**Fig 3I**), and similarly for microclusters of the proximal kinase ZAP-70 (**Fig 3J**), showing that these movements are taking place in association with a stably surface-anchored projection. But, protrusions can also be seen to have more complex merging dynamics, which can result in conglomeration of TCR microclusters when both of the merging contacts are previously occupied (**Movie 8**). Merging takes place even when only one (**Movie 9**) or neither (data not shown) contact contains an evident TCR microcluster, and microclusters themselves can both split and merge (**Movie 10**).

This data provided a framework for correlating membrane protrusion stability with TCR aggregation, and we sought to understand whether signaling and ensuing actin assemblies were required for modulating that stability. To assess this, we first used ZAP70 analog-sensitive(20) OT-I T cells, for which a specific kinase-inhibitor blocks signaling through the proximal kinase in TCR signaling. We found that although drug treatment fully blocked TCR-induced calcium signaling (**Fig 4A,(20)**), both microvillar probing and microcluster accumulation in stabilized contacts was at least as robust as in the absence of signaling (**Fig 4B-C and Movie 11**). Similarly, complete inhibition of all tyrosine phosphorylation with PP2 did not block microvillar scanning but allowed TCR accumulation and associated stabilization (data not shown). In the absence of pMHC (ICAM only on bilayers), 'holes' were observed by SCM (**Fig 4D**) and moved retrograde to

the direction of cell migration (**Fig 4E-F**). Furthermore, stabilization was specific to agonist-bearing complexes and 'null' peptides did not stabilize contacts (**Fig 4G**). While it has previously been observed that tyrosine signaling is not necessary for microcluster aggregation(21), this result shows that cells continue to form microvilli, probe the surface and that TCR occupancy converts these protrusions to long-lived contacts.

To explore this further, we tested the role for the actin cytoskeleton in stabilized contacts. Treatment of recently established synapses with LatrunculinB (LatB), which sequesters actin, results in actin disassembly and the overall loosening of the cell cortex away from the bilayer, as visualized by a decreased interference reflection microscopy (IRM) signal (**Fig 4H and Movie 12**). However, the number of TCR microclusters remained steady after LatB addition even as the number of total contacts decreased to approximate the number of microclusters (**Fig 4I**). Plotting the probability of 'occupancy' of a contact with a microcluster shows that actin depolymerization increases this probability; TCR⁺ contacts are selectively retained over time (**Fig 4J**, see also zoom in **Fig 4H**), both in a single cell and when viewed over many examples (**Fig 4K**). Consistent with this observation, we compared actin localization relative to these contacts in early (<3 minute) synapses with late (>6 minute) synapses in which actin depolymerization clears the majority of the central synapse(4, 15, 22). Whereas early contacts contain high densities of nucleated actin, the actin-void regions in later contacts, particularly of the central synapse, also supported contacts, also consistent with their existence being actin-independent (**Fig S9**). This confirms previous reports that showed actin to be dispensable for existing microclusters to persist(19) and that polymerized actin can be found at early sites of TCR signaling(21). However, it puts those findings in context of clear requirements for actin for most 3D contacts, being compensated for by the presence of TCR microclusters.

While clustering of TCRs has long been proposed to represent a fundamental signaling unit (23, 24), here we see that neither signaling nor cytoskeletal attachment are required for TCR microclusters to complete the search process and capture a membrane contact. It is intriguing that estimates for microvilli dwell times in the absence of ligands was ~3.5-6 seconds, depending on the method used to measure them in this study, since that range is long enough to discern short-lived antagonists (typical $t^{1/2}$ of ~2 seconds) from longer-lived agonist pMHC-TCR complexes(25). Variations in that estimate from LLS to SCM methods may represent the sensitivity of the methods (e.g. with SCM-based tracking of a low intensity signal being susceptible to possible 'dropping' of a contact) and/or the effects of simplified bilayers as compared to complex cell surfaces. While others have recently described immediately-stable 'close contacts'(26) formed on glass surfaces that uniformly induce signaling associated with exclusion of large molecules such as the phosphatase CD45, contacts with native ligands are more dynamics and we did not observe profound CD45 exclusion in most contacts excepting occasional late, central synaptic membrane contacts (**Fig S7E-F**). A series of future questions will need to address how molecules distribute at very small size scales on these tips but the ultimate result may resemble recently described micro-synapses (27). We also speculate that dynamic microvilli are the 3D structure on which previously described lipid rafts or 'islands' are assembled, islands having similar dimensions to microvilli, and that the movements (**Fig 3**) and concatenations (**Movies 8-10**) we describe on 3D surfaces are those on which such islands may merge or split(28). Addressing this will require further updates in microscopy for multi-color LLS at higher frame rates.

Importantly, this work shows that topographic scan, 'palpation' of the opposing surface, underlies the act of TCR recognition and defines a key parameter in cell-cell recognition, namely the time pressure for ligands to solidify interactions with an opposing surface. Given that ligand density is tightly regulated in most biological systems, different cells are expected to take different approaches to this problem and we noted that different immune cell types appear to survey more or less actively as compared to T cells and sometimes with waves or other patterns of membrane movements that are likely to lead to different efficiencies (**Movie 13**). Multiple additional levels of regulation of this process are now open to study.

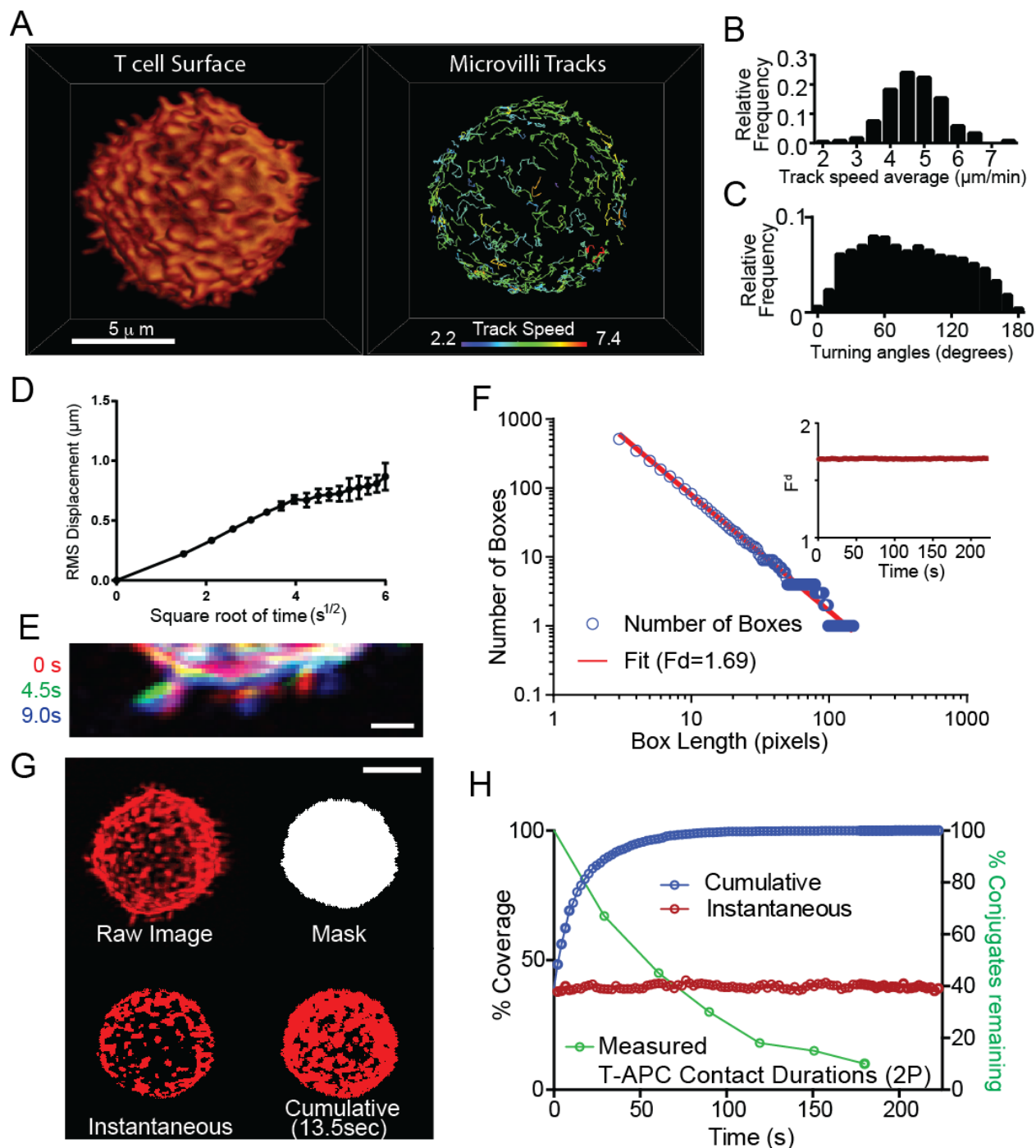


Figure 1. Effective surface scanning by T cell protrusions

A) Surface projection rendering of a mouse T cell imaged by LLS (left). Isolated tracks for individual microvilli (right) See also **Movies 1-2**. Tracking was assisted in some cases by image stabilization, to account for modest cell drift (**Fig S1A**). Scale bar: 5 microns.

B) Track speeds, **C)** Turning angles and **D)** RMS displacement for microvilli ($n=54$ microvilli across 3 cells).

E) Three-color overlay of a sub-section of an isolated T cell at three time points. Scale bar: 1 micron.

F) Fractal Analysis: Plot of the number of boxes needed to cover the active area of a T cell vs. length of the box (L). The slope of the fit line is used to determine the fractal dimension (F_d). Inset: F_d as calculated over time for a single live T cell.

G) Representation of the masking and threshold method used to calculate the instantaneous and cumulative coverage of T cell surfaces and IS ROIs. Anti-CD45 was used to label cell surfaces in this example. Scale bar: 5 microns. See also **Movie 3**.

H) *Left axis:* Percentage of surface coverage (cumulative in blue, instantaneous in red) of an isolated T cell throughout time from LLS *in vitro*. *Right axis:* Percentage of T-APC contacts remaining vs time, from 2-photon imaging data in vital lymph nodes.

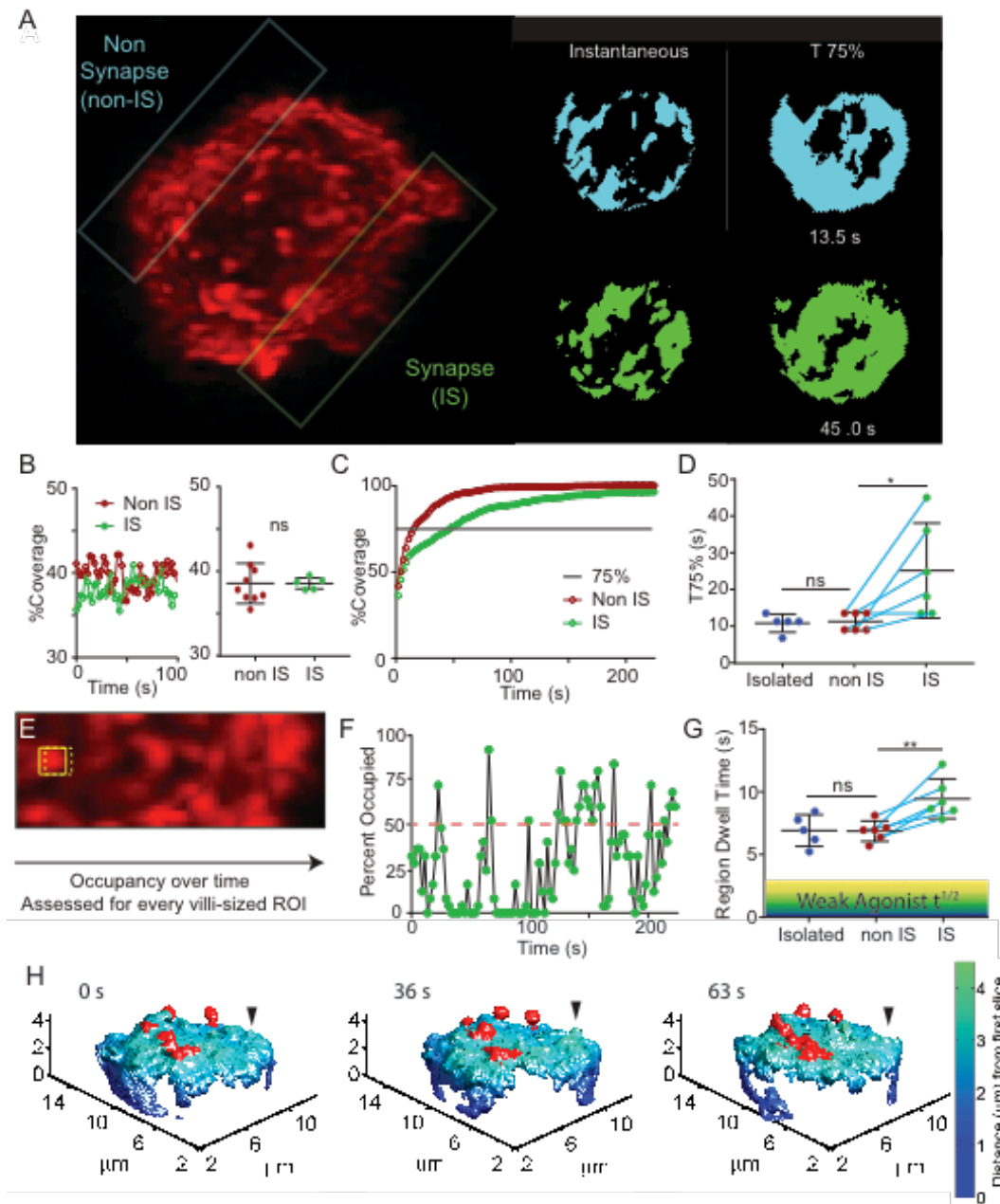


Figure 2. Altered microvillar dynamics in response to ligand detection

A) Left: Image of a T cell in interaction with a peptide-loaded BMDC (unlabeled). The non-synaptic (non-IS) plane of interest is outlined in blue, the synapse (IS) is outlined in green, and the location of the BMDC (APC), taken from high-contrast projection, is indicated in yellow. **Right:** Thresholded images of the non-IS (blue) and IS (green) contact face at a single time point and a cumulative image when coverage had reached 75%.

B) Left: Percent surface coverage throughout time for a non-IS and IS region of a single T cell. **Right:** The distribution of average surface coverage for non-IS regions and IS regions taken from multiple T cells.

C) Percent cumulative coverage comparing the non-IS and IS region of a single T cell. Line indicates 75% surface coverage.

D) Comparison between the distributions of T75% for isolated T cells, non-IS regions, and IS regions of multiple individual T cells.

E) The scanning method for measuring regional dwell time over a contact surface.

F) Variation in occupancy, measured for a 25-pixel sized area, illustrating a cutoff at 50% occupancy. Short lived protrusions are highlighted with the black arrows, while a longer-lived scanning event is shown in gray.

G) A comparison of the average regional dwell time, defined as in F, for isolated T cells, non-IS regions, and IS regions in different T cells. Teal line connects individual cells. Shaded regions denotes generalized half-life for weak-agonist pMHCs.

H) Membrane topology of the synaptic region of a T cell, labeled with anti CD45-Alexa488, interacting with a peptide-loaded BMDC at various timepoints. Stable protrusions are highlighted in red, an example transient protrusion is indicated with a black arrowhead.

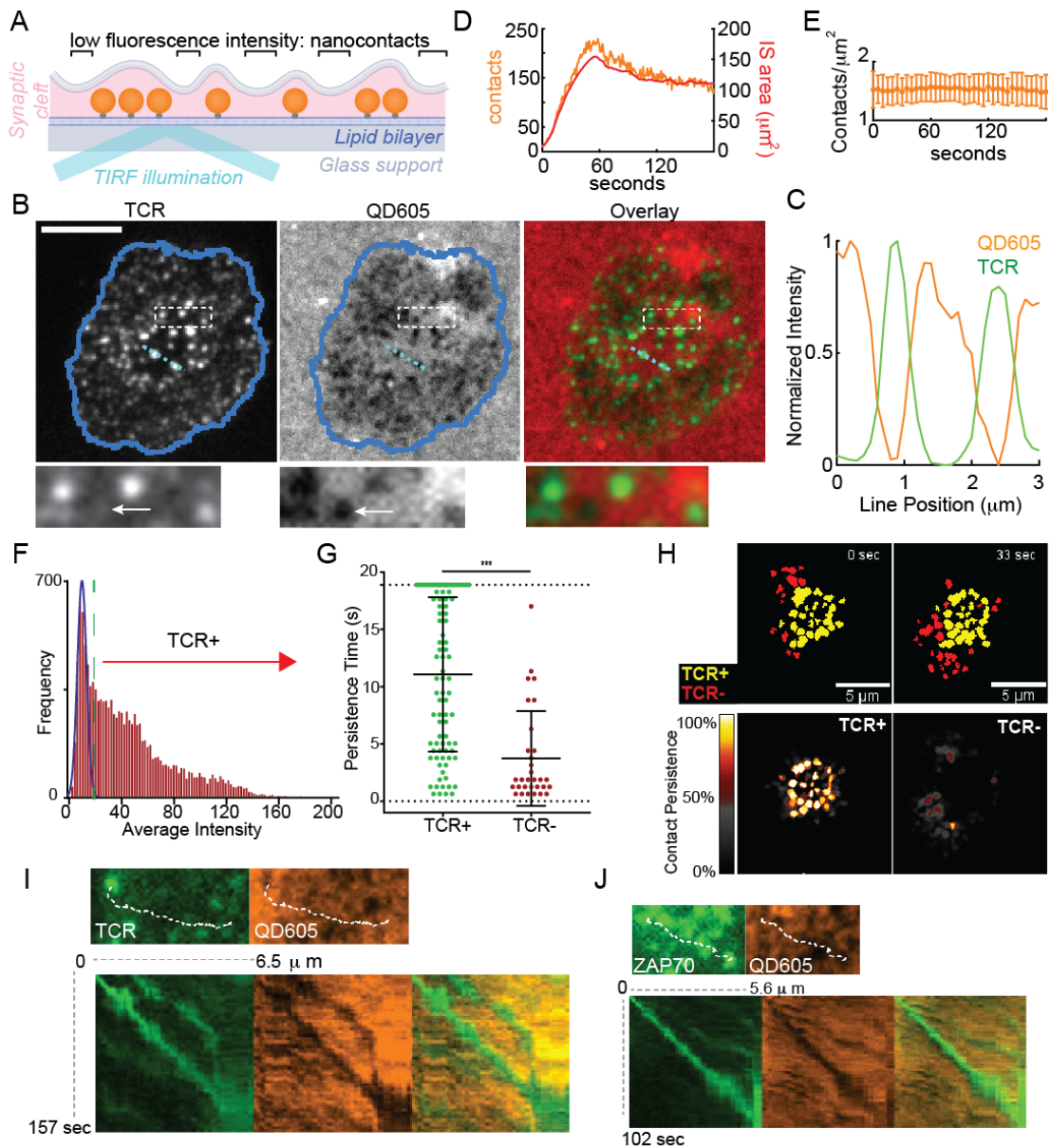


Figure 3. TCR occupied projections are stabilized

A) Schematic representation of bilayer-bound Qdots for SCM based imaging. Note that Qdots larger than the $\sim 15\text{nm}$ TCR-pMHC length are excluded when membranes closely appose. See also **Figure S6-7**.

B) Images of TCRs, bilayer-bound QD605 streptavidin conjugates, pseudocolored streptavidin intensity, and TCR/streptavidin overlays from cells fixed during synapse formation. Scale bars: 5 microns. Region indicated by dashed box in is shown at the bottom. Arrow points to a contact with no apparent TCR microcluster.

C) Normalized intensities of Qdot605 and TCR line scan for the light blue line in (B).

D) Plot of the number of contacts and total IS area during formation of an IS.

E) Plot of average contact density over time during IS formation. Error bars correspond to the standard deviation. Plot represents the average contact density over time for 28 cells pooled from 7 independent experiments.

F) Frequency histogram of the average intensity of all the contacts throughout the observation period. The blue Gaussian curve represents the intensity distribution expected from background sources. The green dashed line represents the cutoff from TCR+ to TCR-.

G) Distribution of dwell times in the TCR+ and TCR- populations within an 18.9 second observation window.

H) Top: Overlay of TCR⁺ (yellow) with the TCR⁻ contact populations (red) at 2 different timepoints. Bottom: Time Projection of TCR+ (left) and TCR- (right). Colors represents the percentage of time of each pixel occupied by contacts over the length of the movie.

I) Top: Image of a nascent H57-labeled TCR microcluster and corresponding contact image. Dashed line indicates the subsequent microcluster path. Bottom: kymographa generated from the microcluster path in each channel and overlay.

J) As I but for a ZAP70-GFP cluster.

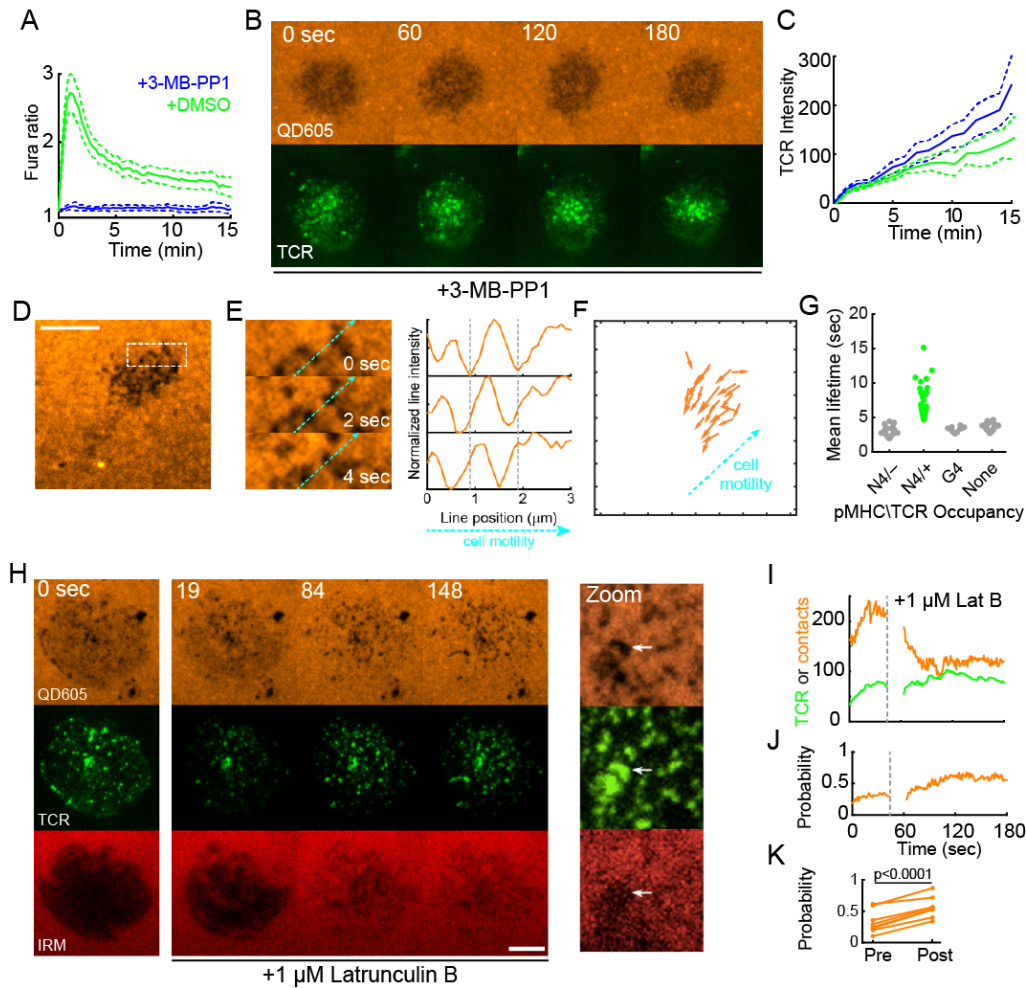


Figure 4. Signaling and cytoskeletal independence of TCR-mediated protrusion-stabilization

A) Fura-2 calcium ratios measured in ZAP70(AS)/OT-I T cells on activating bilayers after treatment with vehicle or 10 μ M 3-MB-PP1. Plots represent the average Fura-2 ratio measured in over 100 cells pooled from 2 separate experiments. Error bar corresponds to the 95% CI.

B) QD605-streptavidin and TCR TIRF time lapse images of ZAP70(AS)/OT-I synapses formed after treatment with 10 μ M 3-MB-PP1. Scale bars: 5 microns.

C) Measured increase in TCR intensity in contacts in ZAP70(AS)/OT-I T cell synapses. 3-MB-PP1: N = 12; DMSO vehicle: N = 9 cells. Data is pooled from 3 experiments. Error bars corresponds to the standard error of the mean.

D) SCM images of bilayer-bound QD605-SA during encounter of OT-I T cell in the presence of bilayer-bound ICAM but in the absence of pMHC. Scale bar: 5 μ m. The boxed region measured 5 μ m \times 2 μ m.

E) Images of contacts in the boxed region shown in D. At right, normalized intensity line scans for the light blue dashed line shown in the images. The vertical gray dashed lines correspond to the starting point along the line for two contacts. The contacts moved against the direction of cell motility.

F) Displacement vectors for tracked contacts shown in the IS in A. For clarity, only tracks longer than 1 μ m are shown. The direction of motility in B and C are indicated by the light blue dashed line.

G) Mean lifetimes for contacts based on the bilayer-bound pMHC complex and TCR occupancy. For the N4, the contacts are categorized based on whether it acquired TCR microclusters. For the G4 and Null conditions, TCR+ microclusters were not observed. Data are polled from at least 3 separate experiments for each condition.

H) Bilayer-bound QD605-streptavidin, TCR and IRM time lapse images of an OT-I IS during Latrunculin challenge. 1 μ M Latrunculin B was added after acquisition of the t = 0 sec image. Scale bar: 5 microns. At right, a zoomed view of a region of the synapse 3 minutes after LatB addition. The white arrow points to a remaining patch of contacts with TCR microclusters and low IRM intensity.

I) Number of contacts (orange) and TCR microclusters (green) before and after Latrunculin challenge for the IS shown in H.

J) The fraction of contacts occupied by TCRs before and after Latrunculin challenge for the IS shown in H.

K) Average fraction of contacts occupied before and after Latrunculin treatment. Each plot point represents the average fraction of contacts occupied in a cell measured over the 60 seconds before (pre-) and after (post-) Latrunculin treatment. N = 7 cells pooled from 3 independent experiments.

References

1. A. M. Glauert, C. J. Sanderson, The mechanism of K-cell (antibody-dependent) mediated cytotoxicity. III. The ultrastructure of K cell projections and their possible role in target cell killing. *Journal of cell science* **35**, 355 (Feb, 1979).
2. U. H. von Andrian, S. R. Hasslen, R. D. Nelson, S. L. Erlandsen, E. C. Butcher, A central role for microvillous receptor presentation in leukocyte adhesion under flow. *Cell* **82**, 989 (Sep 22, 1995).
3. M. L. Dustin, J. A. Cooper, The immunological synapse and the actin cytoskeleton: molecular hardware for T cell signaling. *Nature Immunology* **1**, 23 (2000).
4. S. C. Bunnell, V. Kapoor, R. P. Triple, W. Zhang, L. E. Samelson, Dynamic actin polymerization drives T cell receptor-induced spreading: a role for the signal transduction adaptor LAT. *Immunity* **14**, 315 (2001).
5. J. C. Stinchcombe, G. Bossi, S. Booth, G. M. Griffiths, The immunological synapse of CTL contains a secretory domain and membrane bridges. *Immunity* **15**, 751 (Nov, 2001).
6. S. C. Bunnell *et al.*, T cell receptor ligation induces the formation of dynamically regulated signaling assemblies. *J Cell Biol* **158**, 1263 (Sep 30, 2002).
7. H. Ueda, M. K. Morphew, J. R. McIntosh, M. M. Davis, CD4+ T-cell synapses involve multiple distinct stages. *Proc Natl Acad Sci U S A* **108**, 17099 (Oct 11, 2011).
8. P. T. Sage *et al.*, Antigen recognition is facilitated by invadosome-like protrusions formed by memory/effector T cells. *J Immunol* **188**, 3686 (Apr 15, 2012).
9. A. Pierres, V. Monnet-Corti, A. M. Benoliel, P. Bongrand, Do membrane undulations help cells probe the world? *Trends in cell biology* **19**, 428 (Sep, 2009).
10. B. C. Chen *et al.*, Lattice light-sheet microscopy: imaging molecules to embryos at high spatiotemporal resolution. *Science* **346**, 1257998 (Oct 24, 2014).
11. M. J. Miller, S. H. Wei, I. Parker, M. D. Cahalan, Two-photon imaging of lymphocyte motility and antigen response in intact lymph node. *Science* **296**, 1869 (Jun 7, 2002).
12. M. F. Krummel, F. Bartumeus, A. Gerard, T cell migration, search strategies and mechanisms. *Nat Rev Immunol* **16**, 193 (Mar, 2016).
13. L. Seuront, *Fractals and Multifractals in Ecology and Aquatic Sciences*. (CRC Press, 2009).
14. V. Mendez, D. Campos, F. Bartumeus, *Stochastic Foundations in Movement Ecology: Anomalous diffusion, invasion fronts and random searches*. (Springer Verlag, Gerlin, 2013).
15. P. Beemiller, J. Jacobelli, M. F. Krummel, Integration of the movement of signaling microclusters with cellular motility in immunological synapses. *Nat Immunol*, (Jul 1, 2012).
16. A. Grakoui *et al.*, The immunological synapse: A molecular machine that controls T cell activation. *Science* **285**, 221 (1999).
17. Y. Jung *et al.*, Three-dimensional localization of T-cell receptors in relation to microvilli using a combination of superresolution microscopies. *Proceedings of the National Academy of Sciences* **113**, E5916 (October 4, 2016, 2016).
18. J. M. Alakoskela *et al.*, Mechanisms for size-dependent protein segregation at immune synapses assessed with molecular rulers. *Biophys J* **100**, 2865 (Jun 22, 2011).
19. R. Varma, G. Campi, T. Yokosuka, T. Saito, M. L. Dustin, T cell receptor-proximal signals are sustained in peripheral microclusters and terminated in the central supramolecular activation cluster. *Immunity* **25**, 117 (Jul, 2006).
20. B. B. Au-Yeung *et al.*, Quantitative and temporal requirements revealed for Zap70 catalytic activity during T cell development. *Nat Immunol* **15**, 687 (Jul, 2014).
21. S. Kumari *et al.*, Actin foci facilitate activation of the phospholipase C-gamma in primary T lymphocytes via the WASP pathway. *eLife* **4**, (2015).
22. Alex T. Ritter *et al.*, Actin Depletion Initiates Events Leading to Granule Secretion at the Immunological Synapse. *Immunity* **42**, 864 (2015).
23. R. N. Germain, T-cell signaling: the importance of receptor clustering. *Curr Biol* **7**, R640 (Oct 1, 1997).

24. X. Su *et al.*, Phase separation of signaling molecules promotes T cell receptor signal transduction. *Science* **352**, 595 (Apr 29, 2016).
25. D. S. Lyons *et al.*, A TCR binds to antagonist ligands with lower affinities and faster dissociation rates than to agonists. *Immunity* **5**, 53 (1996).
26. V. T. Chang *et al.*, Initiation of T cell signaling by CD45 segregation at 'close contacts'. *Nat Immunol* **17**, 574 (May, 2016).
27. A. Hashimoto-Tane *et al.*, Micro-adhesion rings surrounding TCR microclusters are essential for T cell activation. *J Exp Med* **213**, 1609 (Jul 25, 2016).
28. B. F. Lillemeier *et al.*, TCR and Lat are expressed on separate protein islands on T cell membranes and concatenate during activation. *Nat Immunol* **11**, 90 (Jan, 2010).

Acknowledgments

Funding for this research was provided by the NIH grant AI052116 to MFK and NSF Graduate Research Fellowship grant 1650113 to CB. We are grateful to Lauren Richie-Ehrlich for the gift of pIB2-Zap70-GFP, and Art Weiss and Byron Au-Yeung for the gift of ZAP70(AS)/OTI mice and the NIH Tetramer Facility at Emory University for the monobiotinylated pMHC monomer reagents.

Author Contributions

PB, KM, CB, EC and MFK designed the experiments. PB and MGR performed the SAIM imaging experiments. PB, EC and CB performed SCM experiments. KM, CB and EC performed the remaining experiments. TL, BC and EB provided critical support for LLS microscopy. VW provided financial support. MFK wrote the paper together with KM, CB and EC.

Competing financial interests

The authors declare no competing financial interests.